Flow, Turbulence and Combustion (2019) 103:1011–1037
https://doi.org/10.1007/s10494-019-00082-4

Gas-Liquid Flow Through an Inclined T-Junction with a Vertical-Upward Branch

Yasmin S. Gavioli[1] · Valter Y. Aibe[1] · Juliana B. R. Loureiro[2]

Received: 26 February 2019 / Accepted: 1 October 2019 / Published online: 12 November 2019

Abstract

The present work studies the behavior of air-water flow mixtures across a 10°-inclined T-junction. A detailed experimental campaign is carried out to yield data on the global and local properties of the gas and liquid phases, including the mass flow rates at the entrance and exits, pressure at several locations, lengths and velocities of the gas bubbles and mean and turbulent statistics of the continuous field. Particle Image Velocimetry and the Shadow Sizer technique are used simultaneously to provide information on the discrete and continuous fields. The gas and liquid flow rates are varied in the ranges $0.07\ \mathrm{m^3h^{-1}} \leq Q_G \leq 0.27\ \mathrm{m^3h^{-1}}$ and $6.07\ \mathrm{m^3h^{-1}} \leq Q_L \leq 13.65\ \mathrm{m^3h^{-1}}$ to define nine different test conditions. Concerning the phase separation efficiency of the investigated T-junction, the observed highest fraction of separated gas was 93%, but with fractions of carried liquid as high as 15% for some conditions.

Keywords T-junction · Two-phase flow · Particle image velocimetry

1 Introduction

1.1 Motivation and objectives

The recent discovery of very large off-shore petroleum reservoirs in Brazil has meant that the production of some single wells may exceed in some cases flow rates of the order of 60,000 barrels of oil per day. One peculiar feature of the produced fluids is the very high content of dissolved gas, in particular, CO_2. As oil flows out of a reservoir, the drop in pressure forces gas out of solution. The resulting oil-gas mixture that arrives at the surface is directed into a separator that channels the oil into a stock tank.

✉ Juliana B. R. Loureiro
jbrloureiro@mecanica.coppe.ufrj.br

[1] Interdisciplinary Center for Fluid Dynamics (NIDF/UFRJ), Federal University of Rio de Janeiro, R. Moniz Aragao No. 360, Bloco 2, 21941-972, Rio de Janeiro, RJ, Brazil

[2] Interdisciplinary Center for Fluid Dynamics (NIDF/UFRJ), Mechanical Engineering Program (PEM/COPPE), Federal University of Rio de Janeiro, R. Moniz Aragao No. 360, Bloco 2, 21941-972, Rio de Janeiro, RJ, Brazil

The use of surface gravity separators frequently implies that very large vessels are required, in many cases not with the necessary fitted capacity to maintain the expected production. Of course, the accompanying large costs of installation and operation also pose additional strain on production. The implication is that large flow separating vessels are progressively being replaced by compact separators that use centrifugal or gravitational forces to provide in-line phase separation. Typically very compact, cyclones and pipe arrays are robust and provide an efficient and low cost separation process.

In many subsea operations, phase separators resort to a combination of cyclones and pipe circuits to promote the segregation of four-phase flows (solid/ liquid/ liquid/ gas). The purpose is to remove the produced sand and water from the oil and gas on the seabed, so as to allow the straightforward re-injection or discharge of the produced water.

The first element in these multiphase flow separators is normally a desander, a cyclone. The second element is a gas-liquid separator consisting of a set of inclined T-junctions sequentially arranged to maximize gravitational effects. The T-junctions are used to separate flows with low to moderate fractions of gas and have the benefit of satisfactorily handling intermittent operational conditions, such as slug flows.

The purpose of the present investigation is to understand the behavior of air-water flow mixtures across a particular type of 10°-inclined T-junction. In the experimental configuration, air-water flow is directed to the entrance of a downward inclined pipe, whose side arm is located in the middle-length of the inclined pipe and is positioned in the vertical direction. The work conducts a detailed experimental campaign, furnishing a database that covers global and local properties of the gas and liquid phases, including, mass flow rates at the entrance and exits, lengths and velocities of gas bubbles and mean and turbulent statistics of the continuous field. Particle Image Velocimetry and the Shadow Sizer technique are used simultaneously to provide information on the dynamics of the bubbles and the continuous velocity field. The gas and liquid flow rates are combined in the ranges $0.07\ \mathrm{m^3h^{-1}} \leq Q_G \leq 0.27\ \mathrm{m^3h^{-1}}$ and $6.07\ \mathrm{m^3h^{-1}} \leq Q_L \leq 13.65\ \mathrm{m^3h^{-1}}$ to define nine different test conditions. The observed highest fraction of separated gas was 93%, but with fractions of carried liquid as high as 15% for some conditions.

Data for two-phase flow entering a T-junction are difficult to find in the literature. The present results provide a very detailed account of the phenomenon, yielding a valuable reference dataset that can be used for any modeling or validation of theoretical or numerical procedures.

1.2 Short literature review

As a two-phase flow enters a T-junction, the phases are unequally split between the upside branch and the main pipeline. Depending on the input conditions, the liquid phase may or may not flow through the lateral branch [1]. Different flow patterns at the junction entrance and the different adopted geometries affect substantially the separation process. Hence, it is of considerable importance to study the mechanisms of phase distributions for different geometries.

A full description of a T-junction can be achieved through the specification of the diameters of the inlet, outlet and upside branch pipes, and their associated angles. The three angles that must be considered are: the pipe angle in relation to the horizontal plane, the angle of the side arm in relation to the pipe and the orientation of the side arm, which can take any angle between −90° (vertically downward sidearm) to +90° (vertically upward sidearm). Azzopardi and Smith [2] investigated the influence of the sidearm orientation and

downstream geometry on the characteristics of the flow separation. The authors observed that, as expected, the amount of liquid separated depends not only on the geometry but also on the inlet flow pattern.

The governing mechanisms of the phase division at a T-junction [3] are very complex because they are influenced by gravity, inertia and pressure forces. Gravity acts on the liquid phase, pushing it downward and minimizing the amount of liquid that is directed upward. Since the axial momentum of the liquid is normally higher than the gas, the liquid is forced to continue flowing downstream the pipe, bypassing the entrance to the side arm. When the sidearm diameter is small, this effect becomes more pronounced since the gas has a short residence time to be influenced by gravity. The typical pressure drop in a T-junction shows a loss between the inlet and the side arm and a recovery inside the run arm. This effect is due to a decrease in the mixture velocity in the run arm, which according to Bernoulli's equation leads to an increase in pressure.

Another critical characteristic of T-junction flows is their transient effects. As remarked by Baker et al. [4], very little work has been conducted in transient flow conditions. Further investigation is thus necessary to elucidate the dynamics behind transient two-phase mixtures across T-junctions.

Pipe junction flows have been consistently investigated since the late seventies. Of particular interest are applications in the nuclear, chemical and oil industry [5–7]. In the review papers of Azzopardi et al. [8, 9], experimental results and physical modelling are discussed separately for annular/stratified flow and stratified/bubbly flows. The works explain that for stratified flow in the entrance of a vertical T-junction, a gas take-off higher than 75% induces waves on the interface that increase the liquid height and eventually forms a hydraulic jump. This phenomenon favors liquid extraction to the vertical branch.

For separation purposes, T-junctions can be set in vertical, horizontal or inclined geometries [10, 11]. Azzopardi et al. [9] discuss the design of horizontal T-junctions for the separation of a vapor/liquid stream that comes from a reactor and is fed to a distillation column. The authors use theoretical modeling and CFD calculations to predict the separation of an annular flow in a pipe of 0.3 m internal diameter, where the liquid is considered to travel as small drops. The effect of pipe diameter and surface tension on Sauter mean diameter of drops is investigated. Separation efficiency is calculated in the range of 51% to 69%.

In the last decades, flow visualization techniques have improved considerably. The use of high speed digital cameras with proper illumination systems permits the measurement of the flow velocity field and phase distribution simultaneously [12]. More recently, researchers have focused on understanding the two-phase flow dynamics inside microchannel T-junctions. Fu and Ma [13] discuss the breakup process of air bubbles in a T-junction microchannel. A visualization study by Yamamoto and Ogata [14] investigates bubble generation and air-water instability in circular microchannels. Results are discussed in terms of the air and water flow rates ratio and include data on bubble length and velocity, slug velocity and frequency of passage. Caprini and collaborators [15] introduce a new design to a microfluidic T-junction, in order to achieve the measurement of all three velocity components in the intersection of two orthogonal planes. A dedicated optical configuration for μPIV is presented. The work shows that a full three-dimensional reconstruction of the velocity field inside the microchannel T-junction can be obtained.

Despite the existing literature, junction flow is not a fully understood problem since a small change in any geometric parameter may significantly affect the flow split. Lahey [16] and Azzopardi [17] mention that up to very recently no satisfactory model existed for the prediction of phase separation over a range of flow conditions and geometrical configurations.

2 Experiments

The experiments were conducted at the Laboratory of Compact Separators of the Interdisciplinary Center for Fluid Dynamics of the Federal University of Rio de Janeiro (NIDF/UFRJ).

2.1 Experimental set up

Figure 1 shows the experimental set up of the present investigation.

The water flow is driven by a progressive cavity pump while the gas phase is provided by a compressed air line equipped with a drying system and pressure regulator valves.

The investigated geometry consists of a Plexiglass pipe with diameter of 70 mm and length of 7.2 m. The pipe is inclined 10° downward. The side branch consists of a Plexiglass pipe (2.4 m in length and 50 mm in diameter) positioned vertically upward at a distance of 4.55 m downstream of the entrance of the inclined pipe. Water and air are fed directly to the inlet of the inclined pipe. The liquid phase is monitored through a sonic flowmeter at the inlet and by a Coriolis mass flowmeter at the outlet of the inclined pipe. The gas phase is measured by vortex flowmeters at the inlet and outlet of the vertical pipe.

A control valve located at the gas outlet can be adjusted to fix the pressure drop on the vertical branch. The mixture that flows downward in the inclined pipe passes through a Coriolis mass flowmeter equipped with a density meter, so that both the gas and liquid phases can be quantified. The water is directed to a secondary reservoir where a level-driven centrifugal pump returns the liquid to the main reservoir.

The experiments are planned so that the flow rates of each phase can be measured on the inlet and both outlets (gas (upward) and liquid (downward) outlets) for the calculation of mass balances and estimation of the separation performance of the T-junction. The transparent walls of the experimental set up permits the use of optical techniques for the measurement of mean and instantaneous velocity fields and for the characterization of the gas phase properties. Absolute and differential pressure transducers are also installed at specific locations.

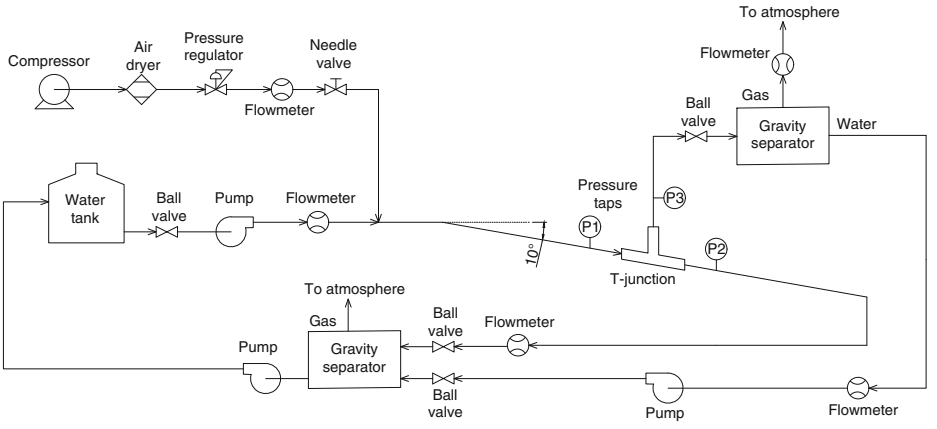

Fig. 1 Overview of the experimental set-up

All pressure transducers and flow meters used in the present work were calibrated against reference instruments. The overall uncertainty for pressure transducers, ultrasonic and Coriolis water flowmeters and gas vortex flowmeters are, respectively, 0.2%, 0.3%, 0.2%, 0.5% of the reading.

2.2 Experimental procedure

The characteristics of the dispersed and continuous phases of the flow were determined through Shadow Sizer System (SSS) and Particle Image Velocimetry (PIV), both systems provided by Dantec Dynamics. To this purpose, two sets of experiments were conducted: i) high speed shadowgraph (SSS) and ii) simultaneous Shadow Sizer and Particle Image Velocimetry. The first set of tests used solely high speed shadowgraph (SSS) to track the deformation of bubbles along the T-junction. The complete sequence of images gives the time evolution of the two-phase flow and allows the observation of the break up and coalescence phenomena. High speed data were also processed to extract information for the calculation of small bubble sizes and bubble velocities distributions. In this case, images were selected from the SSS database in regularly spaced time steps in order to assure statistically independent results. For the second set of experiments, simultaneous Shadow Sizer and Particle Image Velocimetry were used to allow the characterization of the instantaneous velocity fields around well-defined bubbles contours. These measurements were obtained at 15 Hz, maximum Nd:YAG laser shooting frequency. For both sets, the inlet gas flow rates were varied from 0.07 to 0.27 m^3h^{-1} in steps of 0.07 m^3h^{-1}, whereas the inlet liquid flow rates were varied from 6.0 to 13.65 m^3h^{-1}, in steps of 2.0 m^3h^{-1}. These flow rates resulted in different flow patterns on the inclined pipe.

To avoid optical distortions due to the pipe curvature, the T-junction was placed inside a rectangular acrylic box. For the Shadow Sizer measurements, a light diffuser was placed between the acrylic box and the LED light source, in order to obtain a uniform illumination over the entire image. A SpeedSense M310 camera (1280x800 pixels, 3260 fps) fitted with AD Micro-Nikkor 60 mm f/2.8 lens was used for image acquisition. The intensity of the LEDs and lens aperture were adjusted so that the acquired image did not exhibit over or under exposure. Image acquisition frequency varied between 250 Hz to 580 Hz, depending of the liquid flow velocity (the rate increases as the liquid flow velocity increases). Typically, 12,000 images were acquired for each experimental condition.

Image processing was made through a dedicated contour detection algorithm using *MatLab*. A series of image processing operations, including subtraction of the mean background and binarization were applied to make the contour of the bubbles sharply defined. Bubble reconstruction was made with the method described in Matamoros et al. [18]. The use of the contour detection algorithm together with the software "Dynamic Studio" of Dantec Dynamics (version 2015a) allowed the calculation of bubble sizes and velocities, area and perimeter.

For the velocity field characterization, simultaneous 2D 15Hz PIV and Shadow Sizer measurements were performed, as described by the procedure introduced in Nogueira et al. [12]. The system used a SpeedSense M310 camera (1280x800 pixels, 3260 fps) fitted with AD Micro-Nikkor 60 mm f/2.8 lens, a Litron Nd:YAG double pulsed laser with a maximum pulse energy of 150 mJ at 532 nm, repetition rate of 15 Hz, and a LED backlight illumination covered with an orange diffuser, in order to shed light at approximately the same wavelength of the fluorescent particles. The continuous phase was seeded with fluorescent Rhodamine particles, which scatter light in the red wavelength (590 nm). A red filter was fitted to the camera lens to allow the passage of wavelengths above 570 nm, blocking the green laser

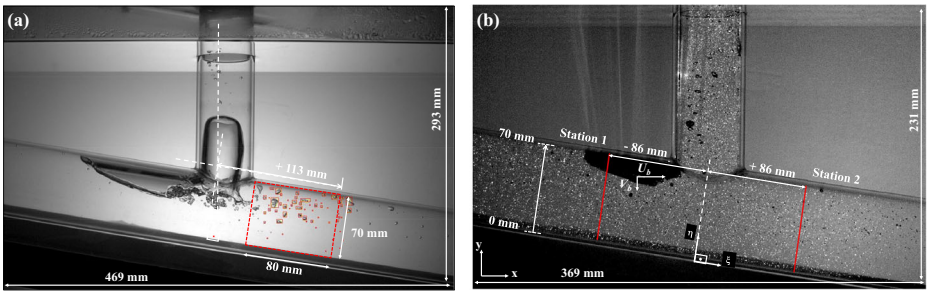

Fig. 2 Field of view and measurement stations for: **a** Shadow Sizer System and **b** simultaneous Shadow Sizer and Particle Image Velocimetry measurements

reflections emitted at 532 nm. The synchronization between the SpeedSense M310 camera, the Nd:YAG double-pulsed laser and the LED system was accomplished so that each frame was simultaneously exposed to both light sources. The acquired images thus contain the seeding particles and well-defined bubble shape information.

The velocity field evaluation was performed with the software "Dynamic Studio" of Dantec Dynamics (version 2015a), through the adaptive correlation routine. This method iteratively optimizes the size and shape of each interrogation area in order to adapt to local flow gradients and seeding densities. The spatial resolution of the PIV measurements is 0.3 mm x 0.3 mm, which was achieved by a series of subsequent analysis using interrogation areas from 32 x 32 to 16 x 16 pixels, with a grid step size of 6 x 6 pixels. The signal-to-noise ratio, defined as the height of the signal peak divided by height of the highest noise peak on the correlation plane, ranged from about 2.5 to 3.5. Post-processing of the velocity field was done with a local 5 x 5 median filter.

The field of view for the two sets of experiments above mentioned, Shadow Sizer System (SSS) and simultaneous PIV and SSS, is shown in Fig. 2a,b, respectively. The region where the measurements of sizes and velocities of small bubbles have been performed are shown in Fig. 2a. Measurement stations for the local liquid velocity profiles are shown in Fig. 2b.

Uncertainties were estimated according to the procedure recommended by the Guide to the Expression of Uncertainty in Measurement [19]. The overall relative uncertainties for small bubble velocity and bubble size are 1.3% and 2% of the reading, respectively. Considering the mass balance calculations, $Q_{G_3} = Q_{G_1}$ has a maximum uncertainty of 10%, $Q_{L_3} = Q_{L_1}$ a maximum uncertainty of 6% and $Q_{L_1} = Q_{G_1}$ a maximum uncertainty of 7%. The subscripts G and L denotes the gas and liquid phases, whose flow rates are measured at the inlet of the inclined pipe (1) and at the outlet of the vertical branch (3), see Fig. 1.

3 Results

This section is divided in four parts: (i) different flow patterns at the inlet are presented and discussed, (ii) the dynamics of bubble break-up and phase separation at the T-junction are analyzed, results for instantaneous and mean liquid velocities, as well bubble size and velocity distributions are introduced, (iii) the flow rate divisions between the liquid and gas outlets are then discussed, (iv) the pressure distribution through the T-junction is shown.

Table 1 Experimental conditions and observed flow patterns on the downward inclined inlet pipe

Test	Flow pattern	Q_{L_1} (m^3h^{-1})	Q_{G_1} (m^3h^{-1})	V_m ($m\,s^{-1}$)	$\Theta = Q_{L_1}/Q_{G_1}$
S1	Stratified	8.0	7.5	1.12	1
S2	Stratified	14.0	7.5	1.55	2
S3	Stratified	8.0	1.7	0.70	5
S4	Stratified	14.0	1.7	1.13	8
EB1	Elongated bubbles	10.09	0.27	0.75	37
EB2	Elongated bubbles	6.07	0.13	0.45	47
EB3	Elongated bubbles	10.09	0.20	0.74	50
EB4	Elongated bubbles	8.05	0.13	0.59	62
EB5	Elongated bubbles	10.09	0.13	0.74	78
EBDB	Elong. & disp. bubbles	11.09	0.13	0.82	86
DB1	Dispersed bubbles	13.65	0.13	0.99	105
DB2	Dispersed bubbles	10.09	0.07	0.73	144

$V_m (= (Q_{L_1} + Q_{G_1})/A)$ denotes the mixture velocity; A is the pipe cross-sectional area

3.1 Flow patterns at the inlet inclined pipe

Early research on two-phase flows devoted considerable attention to the development of flow pattern maps, since prediction of phase distribution is a central problem to many engineering applications.

Important works by Barnea and collaborators [20, 21] particularly focused on two-phase flows in downward inclined pipes. Theoretical models were then introduced as to correctly account for the start of wavy stratified pattern in downward flow. Due to the gravity force, the liquid exhibits a lower level in the pipe and moves faster in the downward inclined case as compared with the horizontal configuration. As a consequence, the stratified flow region in the flow pattern map is expanded as the angle of inclination increases, and is always wavy or ripply for angles above 5° for pipes with 51 mm diameter [21].

For the ranges of inlet gas (Q_{G_1}) and liquid (Q_{L_1}) flow rates investigated in the present work, four different flow patterns were observed at the inlet pipe (Table 1).

For the highest flow rates – in the range $8\ m^3h^{-1} \leq Q_L \leq 14\ m^3h^{-1}$ and $1.7\ m^3h^{-1} \leq Q_G \leq 7.5\ m^3h^{-1}$ – a stratified flow pattern at the entrance is observed, much in accordance with the predictions of Barnea et al. [21]. As shown in Fig. 3a, the stratified flow pattern remains valid in the downward inclined inlet pipe until the T-junction is reached. At this point, a fraction of the gas is directed towards the vertical branch to the upper outlet.

Though flow pattern maps are typically expressed in terms of gas and liquid superficial velocities, Spedding and Nguyen [22] suggest that the liquid-gas volumetric flow rate ratio, Q_L/Q_G (= Θ), and the Froude number are the most appropriate parameters to be used for map representation. As shown through Table 1 and Fig. 3, this notion is useful for classification of the presently studied flow patterns. Indeed, as the liquid-gas flow rate ratio is observed to increase, the flow pattern at the inlet is also observed to change consistently through 4 patterns: stratified, elongated bubbles, elongated and dispersed bubbles, dispersed bubbles. For low Θ, buoyancy effects are significant; for high Θ, dynamic pressure effects are prevalent.

For the present geometrical configuration (pipe diameter = 70 mm and inclination angle of 10°), stratified flows were always noted for $\Theta \leq 8$. An increase in Θ at the inlet pipe leads

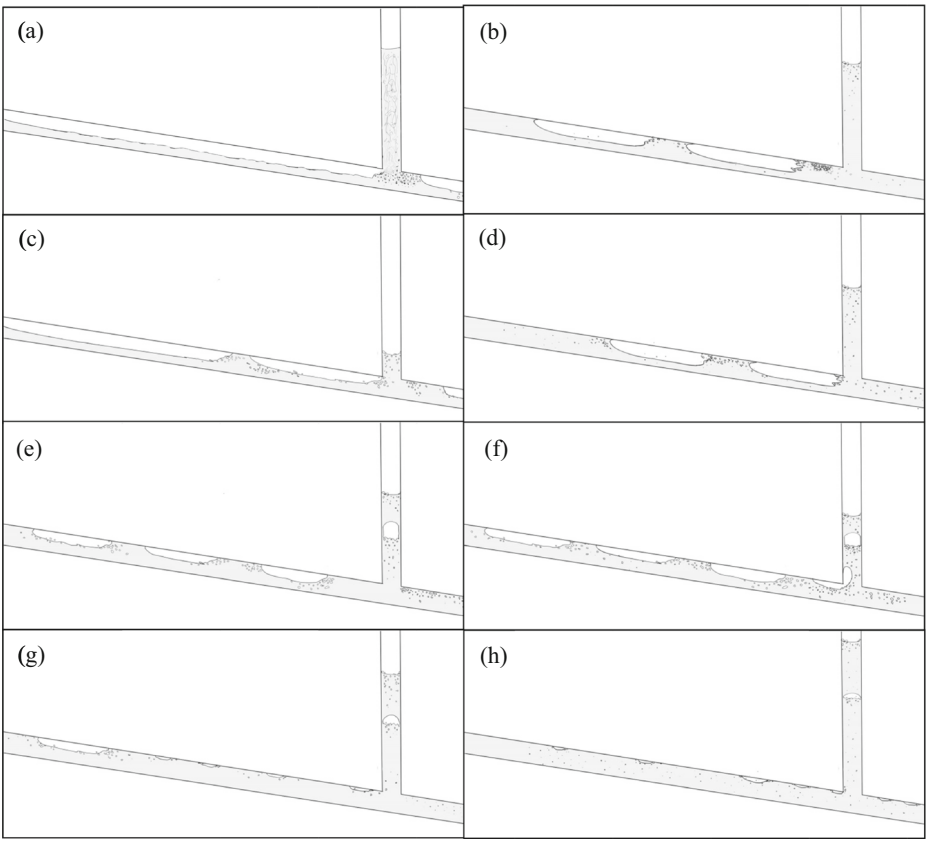

Fig. 3 Typical flow patterns along the T-junction for experimental conditions listed in Table 1: **a** S1 to S4 (stratified flow), **b** EB1 (elongated bubbles), **c** EB2, **d** EB3, **e** EB4, **f** EB5, **g** EBDB (elongated and dispersed bubbles) and **h** DB1 and DB2 (dispersed bubbles). Flow is from left to right for the inclined pipe and from bottom to top for the vertical pipe

to a change from stratified to elongated bubble flow pattern. The momentum of the liquid phase combined with gas fraction give origin to a phase distribution where the noses of the long bubbles are oriented upward, in the opposite direction to the inlet flow. The balance between drag (pressure) and gravity forces is stable and, as a result, the mean position of the elongated bubbles is relatively steady in time. For the present experimental conditions, different configurations of stable elongated bubbles were observed for the range $37 \leq \Theta \leq 78$, as shown in Fig. 3.

Kokal and Stanislav [23] claim to have been the first to report this steady regime in the literature, and denoted this flow pattern as "wave flooding". This regime is observed only for downhill flow at low gas and intermediate liquid velocities. The work notes that the downward two-phase flow is more complex as compared with upward flow and the observed flow pattern varies significantly with pipe inclination and diameter. Despite a relatively common occurrence in practical engineering applications, this type of flow has not received much attention.

For a large range of the present test conditions, the two-phase flow patterns were relatively stable, much as the flow patterns reported by Kokal and Stanislav [23]. The large

bubbles in the inclined pipe are always subject to gravity and pressure forces. Upon the prevalence of the gravity forces, the bubbles tend to move upstream. Of course, dynamic pressure forces tend to push the bubbles in the other direction, downstream. The complication is that a train of observed large bubbles (see, e.g., Fig. 3f) is affected not only by the aforementioned effects, but further by (i) the intermittent incoming flow, (ii) small bubbles coalescence and break up (at the nose and tail regions of the large bubbles) and (iii) the lengths of the liquid slugs. Implicit here is the strong dependence of the behavior of large bubbles on the turbulence level of the flow.

Depending on a combination of the several above listed effects, bubbles may remain located at relatively stable positions or eventually move upstream or downstream. Moving bubbles can in time be captured by the vertical pipe and separated from the flow.

Some of the observed flow patterns are discussed next with Fig. 3 as a reference. The dynamics of bubble coalescence and break up is discussed in a separate section.

One clear and important aspect of the separation process of two-phase flow in an inclined pipe is the manner in which large bubbles negotiate coalescence at their noses and break up at their tails. Provided small bubbles enter and leave a large bubble at the same rate, the large bubble tends to remain steady. Once this balance is broken, a large bubble may grow or decrease in size and make its way into the vertical pipe and out of the system. A bubble that leaves the system is replaced by a new one and the process is repeated. The separation process is then cyclic, with the *irregular* periods depending strongly on the coalescence rate (and break up) that dictates the bubble growth.

The drawings shown in Fig. 3 were prepared from low magnification images of the whole inclined pipe provided by the high speed camera. These drawings show the typical phase configurations that were observed from the experimental conditions reported in Table 1 at the initial stages of separation. All the reported test conditions showed great repeatability.

Figure 3b–f illustrate the observed elongated bubble flow patterns (see also Table 1). Two elongated bubbles connected by a liquid slug are noted on Fig. 3b. This flow pattern was obtained by making $\Theta = 37$ and $V_m = 0.75$ ms^{-1}, where the mixture velocity of the flow is defined as the total volumetric flow rate divided by the inlet pipe cross-sectional area ($V_m = (Q_{L_1} + Q_{G_1})/A$). The bubble wake is characterized by the presence of many dispersed small bubbles. The liquid slug between the large bubbles also shows dispersed bubbles, which due to the buoyancy forces are kept on the upper part of the inclined pipe.

Because the flow pattern configuration was stable, the sizes of long bubbles and liquid slugs could be directly measured through a ruler installed on the pipe wall. The results are shown in Table 2, where "first bubble" denotes the bubble located nearest to the pipe

Table 2 Length of elongated bubbles (L_f) and liquid slugs (L_s) for different liquid-gas flow rate ratios (Θ)

Test	Θ	First L_f/D	First L_s/D	Second L_f/D	Second L_s/D	Third L_f/D
EB1	37	2.40	0.83	2.54	x	x
EB2	47	3.11	0.43	2.17	x	x
EB3	50	2.07	0.83	1.89	x	x
EB4	62	1.89	0.61	1.67	0.61	1.29
EB5	78	1.60	0.83	1.44	0.90	1.67
EBDB	86	1.30	x	x	x	x

D denotes the inlet pipe diameter (= 70 mm)

inlet. Due to the flow unsteadiness, the noses and tails of bubbles were observed to drift about 30 mm in position for some extreme conditions. To avoid measurement errors, a synchronization system was used so that the nose and tail positions were captured at the same time. The typical uncertainty for bubble length measurement was 0.5 mm.

For the test configuration EB1, with $\Theta = 37$ and $V_m = 0.75$ ms^{-1}, two elongated bubbles with lengths of $2.40D$ and $2.54D$ were observed.

For the experimental condition EB2, the mixture velocity decreases and Θ increases in comparison to EB1. The lower liquid and gas velocities favor buoyancy forces, so that bubble sizes are larger than those measured for EB1 (see Table 2). The low liquid level on the vertical branch of the T-junction is due to the low inlet liquid flow rate. The length of the downstream bubble progressively increases as a result of the coalescence of small gas bubbles that are shed from the tail of the upstream bubble. The length of the upstream bubble remains stable since the rate of gas shed from its tail is the same as the coalescence of incoming small bubbles at its nose. As the length of the downstream bubble increases with time, the bubble eventually reaches the vertical branch of the T-junction, where a portion of gas is separated. The cyclic process re-starts with the growth of the elongated bubble that is stably located upstream of the junction (Fig. 3c).

Test EB3 presented a similar behaviour to EB1. Two elongated Taylor bubbles were noted with slight differences in sizes and locations as shown in Fig. 3d.

A further increase of Θ, in the range of 62 to 78 (tests EB4 and EB5), resulted in the appearance of a third stable bubble, as shown in Fig. 3e,f. Though the tests EB1, EB3, EB5 and DB2 have similar mixture velocities, the observed flow patterns are different. This observation shows the usefulness of the liquid-gas flow rate ratio (Θ) as a relevant parameter for flow pattern characterization [22] in inclined T-junctions.

Table 2 shows that for $\Theta = 86$ a transition regime between elongated bubbles and dispersed bubbles takes place. The Taylor bubble has a length of $1.30D$, a smaller value than those observed for the EB's flow patterns. The downstream portion of the inclined pipe is occupied by dispersed small bubbles with a few millimeters in diameter, which tend to be located at the upper wall due to buoyancy effects (Fig. 3g). For Θ larger than 100, only dispersed bubbles were observed (Fig. 3h).

3.2 Dynamics of bubble separation and break up at the T-junction

In the following, the high speed images obtained through the Shadow Sizer System are discussed. Consecutive images are presented so as to permit an interpretation of the time evolution of the flows. The interfaces of the long bubbles were particularly identified to track the bubble break up process around the T-junction. High speed shadowgraph images were also processed to extract statistically independent information for the calculation of small bubble sizes and distributions.

Instantaneous and mean velocity fields obtained through 15 Hz, 2D-PIV are also shown. These results are used to further understand the dynamics of gas separation at the T-junction. In particular, the flow recirculation regions and the locations of high Reynolds shear stress are shown.

To discuss the gas separation behavior for every type of inlet flow pattern introduced in the previous section, results for the tests EB2 and EB4 (elongated bubbles), EBDB (transition elongated bubbles-dispersed bubbles) and DB1 (dispersed bubbles) are next discussed.

Figure 4 shows the phase configuration around the T-junction for the experimental condition EB2 (Table 1). The measurements were performed with the Shadow Sizer System set

Fig. 4 Dynamics of bubble separation at the T-junction: high speed images for experimental condition EB2 (elongated bubbles). Frequency of acquisition is $f_{aq} = 250$ Hz. Time interval between the above images = $10 f_{aq}^{-1}$

to an acquisition frequency (f_{aq}) of 250 Hz. The time step between the presented images is 10 f_{aq}^{-1} and the field of view is 469 mm width and 293 mm in height.

As illustrated in Fig. 3c, the inlet flow pattern for this experimental condition is defined by two steady elongated bubbles upstream of the T-junction. Note that the field of view of the images shown in Fig. 4 is small and centered around the T-junction, to permit a good resolution for the evaluation of the bubble statistics.

The time evolution shown in Fig. 4 illustrates the intermittent behavior of the gas phase separation process in the investigated T-junction. Starting from a stable condition, Fig. 4i, the wake of the elongated bubble located upstream of the T-junction (see Fig. 3c and Table 2) sheds small bubbles, of few millimeters in diameter, that occupy most of the cross section of

the pipe. The liquid level inside the vertical branch is located at the top limit of the image. The pressure and buoyancy effects separate just a portion of bubbles that are located near the upper wall of the inclined pipe. Most of air bubbles that are carried downstream coalesce and grow in size, giving birth to an elongated bubble downstream of the T-junction (Fig. 4i to xiii).

Intermittent flow can also be noted through oscillations on the level of liquid in the vertical pipe. As the liquid level moves upward (Fig. 4x to xiv) small bubbles separate from the main stream, coalescence in the vertical branch and are separated. However, as the vertical liquid column moves down, Fig. 4v to viii, the bubbles are observed to largely remain in the inclined pipe. Figure 4ix to xii show that most of these small bubbles coalescence onto a downstream large bubble. The elongated bubble that forms downstream of the T-junction grows in size with time, Fig. 4xiii to xix, and is displaced upstream through buoyancy effects, onto the T-junction direction. The changes in the vertical liquid level also influences the behavior of the elongated bubble in the neighborhood of the T-junction (Fig. 4xix to xxii). The increase in size occurs until the elongated bubble is fully captured by the vertical pipe and a new cycle restarts (Fig. 4xiv to xxviii).

To illustrate the separation process of an upstream elongated bubble, the experimental condition EB4 is also discussed here. Figure 5 shows the phase distribution around the T-junction for $\Theta = 62$. For the high speed camera, an acquisition frequency (f_{aq}) of 250 Hz was used. The time step between the presented images is $10\,f_{aq}^{-1}$ and the field of view is 469 mm width and 293 mm in height.

Due to the limited field of view, just the bubble tail is seen in Fig. 5i. The wake region shows a high void fraction and, much as in the previous description, small bubbles that are shed downstream are only partially separated at the junction. The main difference in comparison to the previous configuration is the unsteadiness of the vertical liquid level. As illustrated in Fig. 3e, the stable liquid level on the vertical branch is higher, and this

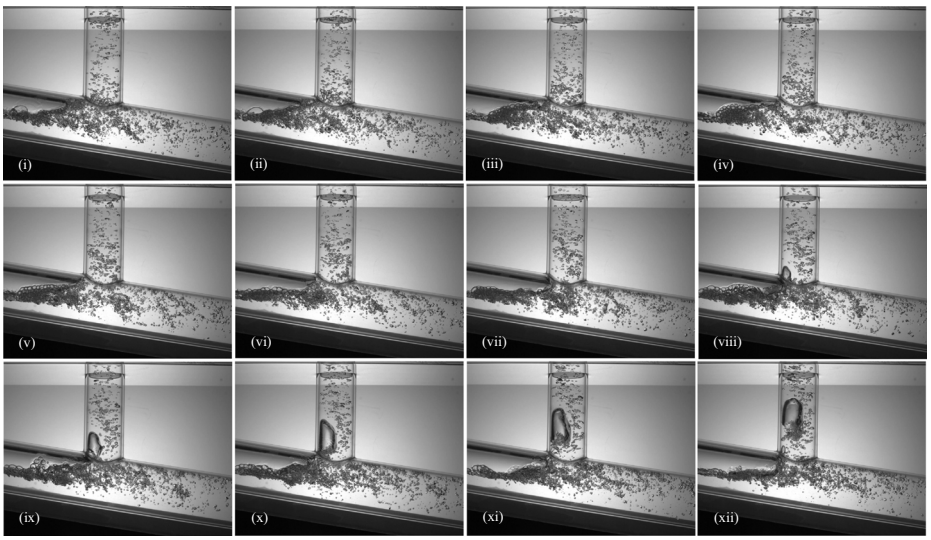

Fig. 5 Dynamics of bubble separation at the T-junction: high speed images for experimental condition EB4 (elongated bubbles). Frequency of acquisition is $f_{aq} = 250$ Hz. Time interval between the above images = $10\,f_{aq}^{-1}$

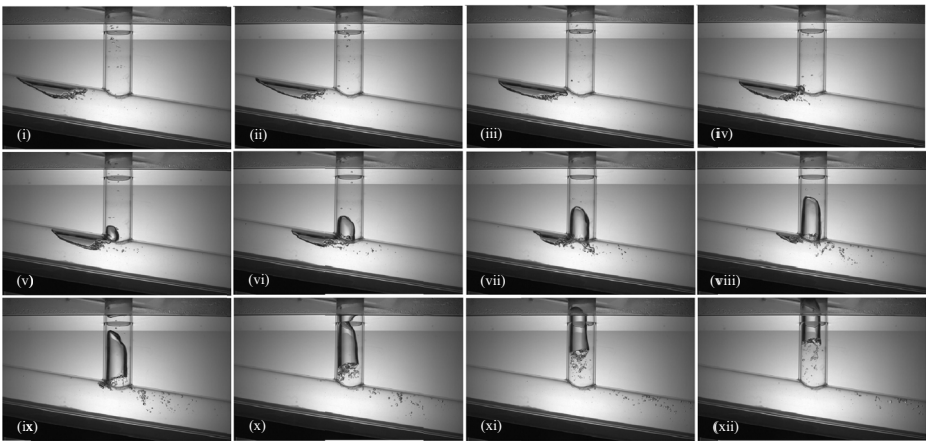

Fig. 6 Dynamics of bubble separation at the T-junction: high speed images for experimental condition EBDB (elongated and dispersed bubbles). Frequency of acquisition is $f_{aq} = 300$ Hz. Time interval between the above images = $10 f_{aq}^{-1}$

contributes to an elimination of the oscillations. Figure 5i to xii show that the bubbles that reach the vertical pipe are always directed up and out of the system. In their movement, a small swirl is noted. The bubbles that flow in the inclined pipe do not coalesce. Owing to their small sizes, they tend to remain finely dispersed across the pipe diameter.

For the elongated-dispersed bubbles flow pattern, the features of the phase separation process are shown in Fig. 6. The elongated bubble located upstream of the junction is observed to be shorter than those described for the other conditions (Table 2), has a slim shape and undisturbed surface. The bubble wake region is short and scarcely aerated. The few dispersed bubbles flow near to the top surface of the inclined pipe and are easily separated, Fig. 6i,ii.

Pressure forces push the elongated bubble downstream of the inclined pipe to the entrance of the T-junction (Fig. 6iii to vi). As this point, much of the bubble's volume penetrates the vertical pipe. However, the high levels of turbulence and shear at the rear of the formed vertical bubble (see Figs. 10 and 12), break the tail into a considerable number of small bubbles that are carried downstream of the pipe (Fig. 6iv to vi). The short time plugging of the vertical pipe by the escaping large bubble helps the small detached bubbles to flow downstream. In fact, as the large bubble in drawn into the vertical pipe, the high dynamic pressure forces (and the resulting acceleration) on the bubble volume that remains in the pipe combined with the high turbulence levels in the tail wake promote further bubble break up (Fig. 6vii to ix), giving rise to further small bubbles that are carried away from the junction. The long bubble in the vertical pipe freely flows up, with the small trailing bubbles quickly coalescing at its rear (Fig. 6x to xii).

The separation process for dispersed bubbles of moderate sizes is shown in Fig. 7. The phenomenon is considerably simpler than the one just described in the previous paragraph but one salient feature is of great importance. Dynamic pressure forces drive a moderate size bubble downstream, onto the entrance of the junction (Fig. 7i to vi). At the entrance, the bubble is strongly deformed and, for a short time, occupies most of the pipe opening (Fig. 7vii). Upon the action of gravity, most of the bubble's volume penetrates the vertical pipe, but not before small bubbles break away from the main body (Fig. 7viii). In fact, two

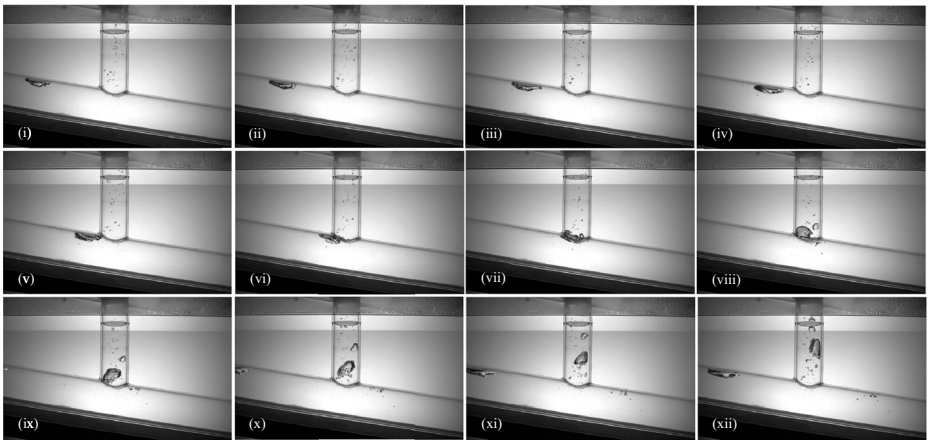

Fig. 7 Dynamics of bubble separation at the T-junction: high speed images for experimental condition DB1 (dispersed bubbles). Frequency of acquisition is $f_{aq} = 430$ Hz. Time interval between the above images = $10 f_{aq}^{-1}$

bubbles of moderate size are also visible in Fig. 7viii as a result of the break up process. The smaller bubble rises freely whereas small bubbles are further observed to break up from the larger bubble (Fig. 7ix to xi). Figure 7xii shows the arrival of a new bubble of moderate size and the start of a new cycle.

Figures 4, 5, 6 and 7 have shown the time evolution of bubble separation at the T-junction for some of the different inlet flow patterns studied in the present work. To all cases, phase separation occurs in relatively steady cycles. The separation cycles start from some given configuration (Fig. 3), evolve as dynamic and gravity forces move the bubbles toward the T-junction and is ended after the separation process occurs. With the income of new bubbles, the cycle re-starts.

For a better illustration of the break up process, the contour of a single bubble is isolated and tracked through its motion. This procedure is applied just for the transition (EBDB) and dispersed bubbles (DB1) inlet flow patterns. These are especially attractive cases for this type of analysis due to the small gas fraction that is involved in the definition of the flow patterns. The low amount of gas is essential to permit a correct identification of the daughter bubbles that are formed with the fragmentation process.

Figures 8 and 9 show the contour of a single long bubble (in red) and the temporal evolution of the process of break-up. The daughter bubbles are illustrated in different colors, where each color is used to denote a fragmentation event. The stretching and pulling mechanism that results in break-up begins at the tail of the long bubble and is amplified by the shear layer that bounds regions of high and low velocities. The regions of slow and fast moving fluid are clearly identified in Figs. 10 and 11 for conditions EBDB and DB1, respectively. Daughter bubbles that further suffer fragmentation are represented through the same color.

Instantaneous velocity vector fields obtained through the PIV measurements are shown in Figs. 10 and 11 for the test conditions EBDB and DB1, respectively. To illustrate the bubble location, the vector fields were superposed to the images obtained from the simultaneous PIV and Shadow Sizer measurements. The reference velocity magnitude is shown on the top right of the figures. Velocity magnitudes can be further visualized through the color scale

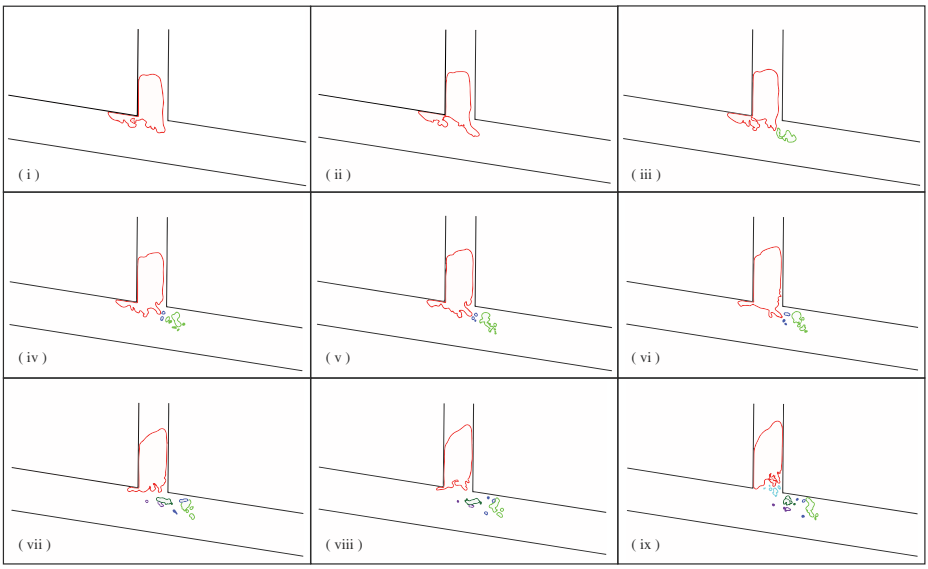

Fig. 8 Bubble contours illustrating the break up process for transition inlet flow pattern (EBDB). Time interval between images is 13 milliseconds

on the right hand size of the figures. Streamlines are shown to improve visualization of the flow recirculation regions. The PIV measurements were especially important to characterize the dynamics of flow separation.

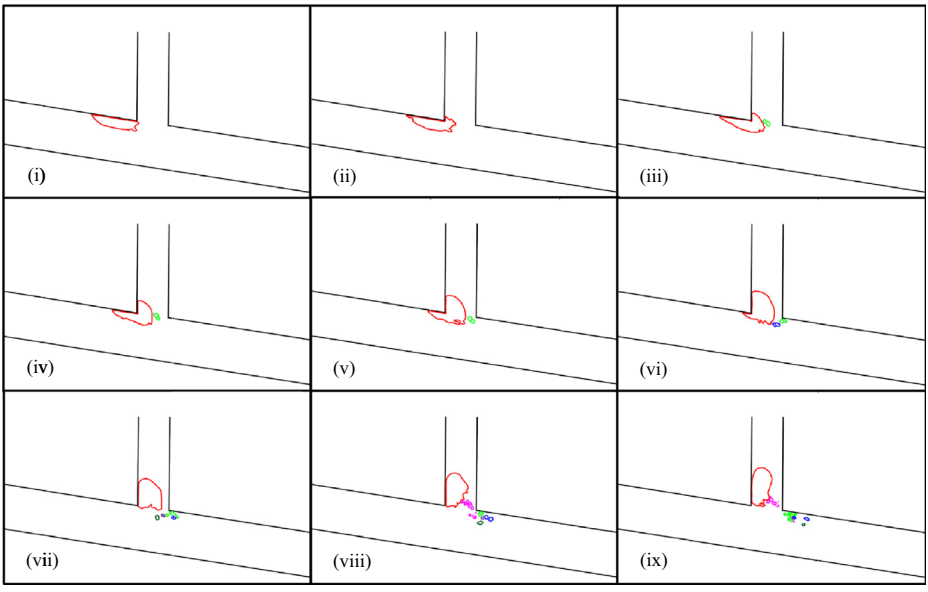

Fig. 9 Bubble contours illustrating the break-up process for dispersed bubbles inlet flow pattern (DB1). Time interval between images is 28 milliseconds

Figures 10a–c illustrate a long bubble flowing through the vertical branch. As the gas phase separation occurs and the bubble deforms, a region of low velocity takes place downstream of the junction, illustrated by the closed streamlines in Fig. 10a. Figure 10b shows the instantaneous velocity field for a break up event (EBDB condition). The same event is described through the shadowgraph images of Fig. 6vii and the isolated contours of Fig. 8ii,iii. In particular, a moderate size bubble in the wake of the long bubble is observed to be stretched by the shearing effects of the flow. This stretching mechanism persists until the long bubble enters the vertical branch (Fig. 10b–e) and the undisturbed incoming flow

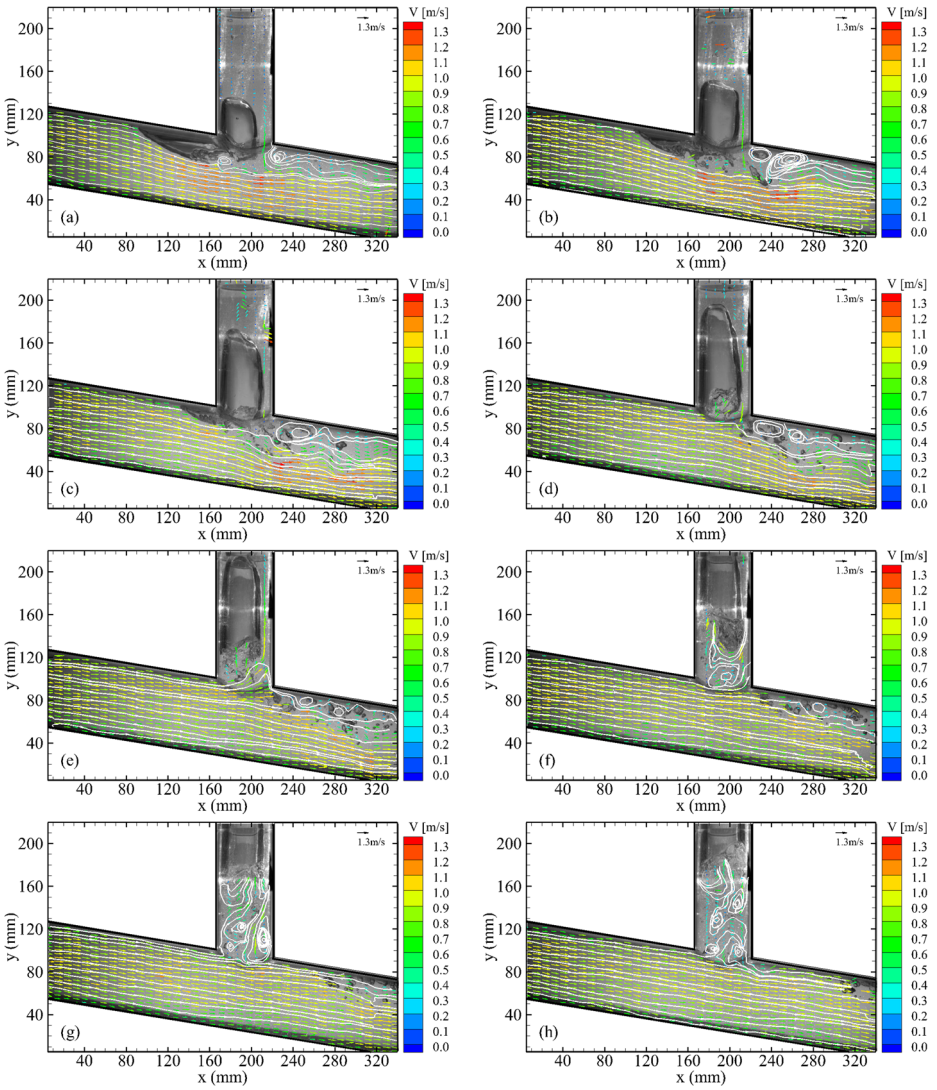

Fig. 10 Instantaneous velocity fields superposed on shadowgraph images for condition EBDB. Velocity vectors are color coded according to their magnitudes (V[ms^{-1}]). Streamlines are shown in white. Time interval between images is 67 milliseconds

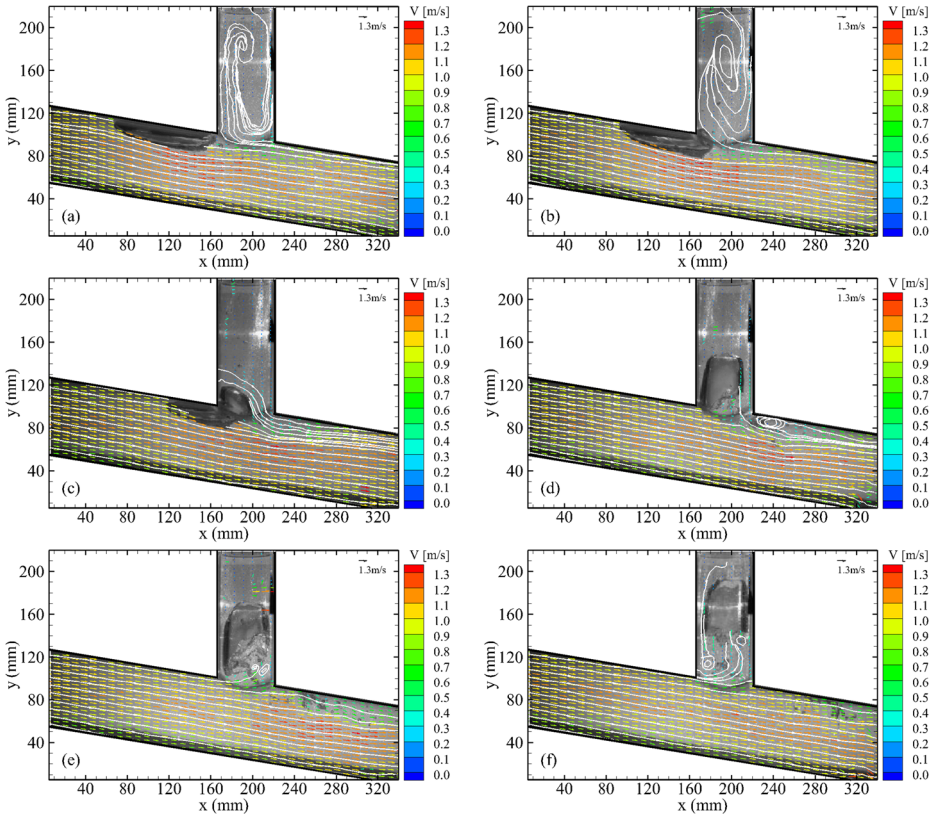

Fig. 11 Instantaneous velocity fields superposed on shadowgraph images for condition DB1. Velocity vectors are color coded according to their magnitudes (V[ms^{-1}]). Streamlines are shown in white. Time interval between images is 67 milliseconds

reaches the downstream upper wall of the junction (Fig. 10f–g). Dynamic pressure forces carry the smaller daughter bubbles downstream of the inclined pipe. Regions of low velocity are also noted in the wake of the long bubble inside the vertical branch.

A similar behaviour is observed for a short isolate bubble that occurs in the disperse flow pattern (as shown in Fig. 11 for the condition $\Theta = 105$ (DB1)). These bubbles, despite their relative small sizes are also subject to break up. Once a bubble is deformed into the vertical branch (Fig. 11c) a low velocity region is formed downstream. Figure 11d,e show that a small recirculation region is observed as the bubble is captured by the vertical branch. As the bubble rises up the undisturbed flow condition is reestablished (Fig. 11f).

Figures 12 and 13 show the measured mean Reynolds shear stress for conditions EBDB and DB1, respectively. Phase discrimination was considered for the evaluation of the averaged values. Figures 12 and 13 corroborate the phenomenology description implied by Figs. 10 and 11, respectively. The regions of high Reynolds shear stress show the locations most likely for a break up event to occur (see Figs. 8 and 9).

The above described break up process was typically observed for all the inlet flow pattern conditions: “elongated bubble”, “transition” and “dispersed bubbles”. Once a large bubble is separated at the junction, smaller daughter bubbles are formed due to the effects resulting

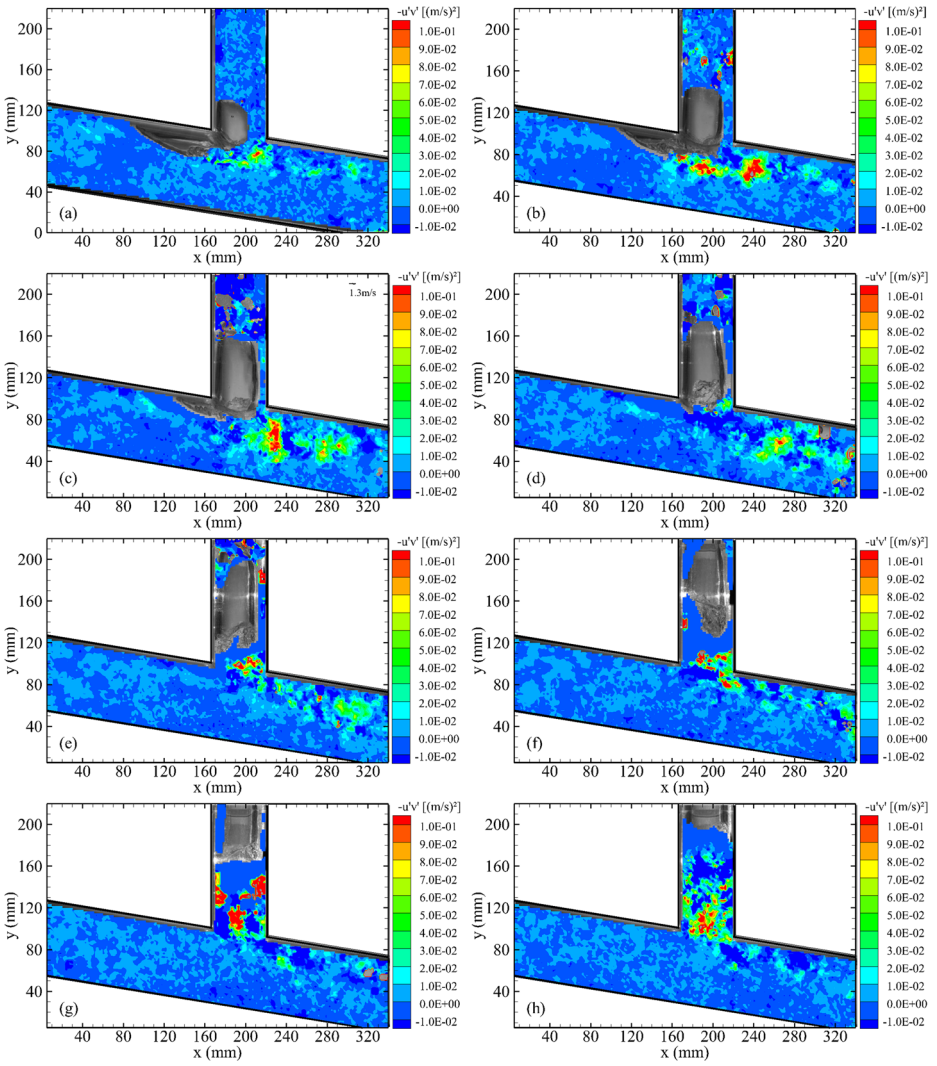

Fig. 12 Reynolds shear stress fields superposed on shadowgraph images for condition EBDB. Time interval between images is 67 milliseconds

from shearing and high turbulence provoked the general flow configuration including the wake region (illustrated by the closed streamlines). Figures 10, 11, 12 and 13 show that the low velocity recirculation region is unsteady; it is formed as a long bubble is captured by the vertical branch and eventually fades away as the dynamic pressure of the incoming liquid flow drags the small bubbles downstream of the inclined pipe. This phenomenon is repeated in time; Figs. 10 and 11 illustrate the typical instantaneous velocity field for one cycle, which corresponds to the separation of one long bubble. Considering the design of a separation equipment, this phenomenon imposes a serious drawback since small bubbles are always being created and, thus, are not separated.

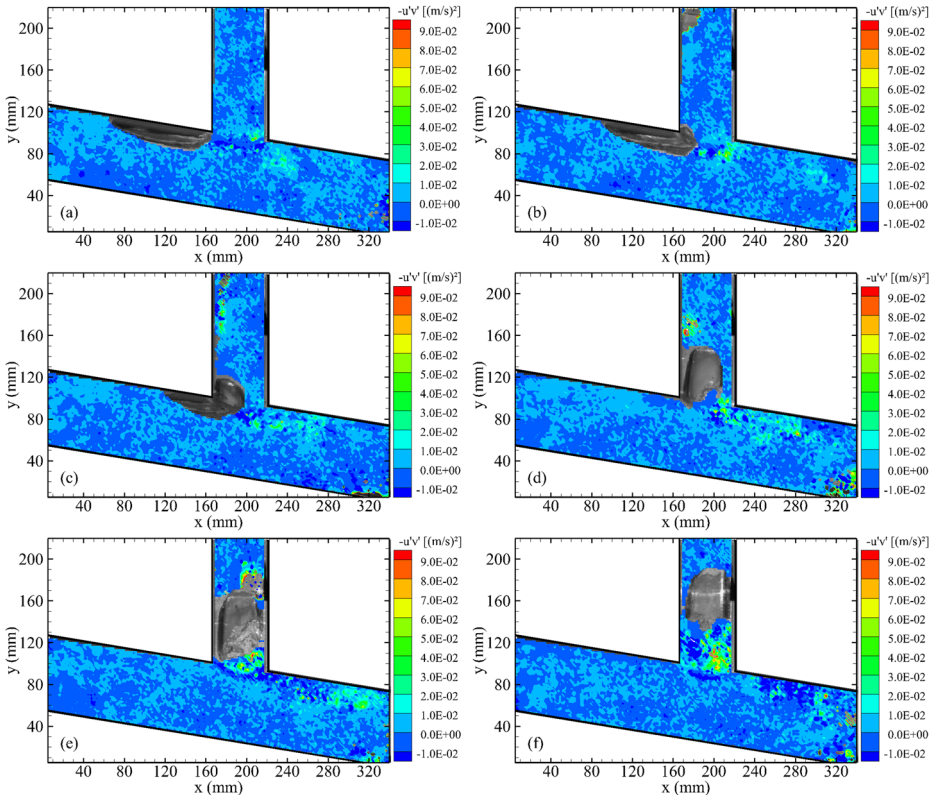

Fig. 13 Reynolds shear stress fields superposed on shadowgraph images for condition DB1. Time interval between images is 67 milliseconds

Mean velocity profiles at stations 1 and 2 (Fig. 2) located respectively $\eta = -86$ mm (upstream) and $\eta = 86$ mm (downstream) of the T-junction, are shown in Fig. 14 for conditions EB1 to DB2 (Table 1). Profiles were extracted perpendicularly to the pipe wall. Of course, the general shape of the mean velocity profiles is intrinsically related to the position of the bubble upstream of the junction.

For the test conditions EB2, EB4 and EB5, the long bubbles are stably positioned immediately upstream of the T-junction. The coalescence of small bubbles at the large bubble nose permits the bubble to grow in size until separation through the vertical branch eventually takes place. Soon after separation, a new bubble grows and replaces the previous bubble at the same location.

The mean velocity profile for condition EB2 shows that the mean liquid height at that location corresponds to 40% of the pipe diameter. For conditions EB4 and EB5, the mean velocity profiles show an inflection. The inflection point separates the high velocity region near the bottom wall of the inclined pipe ($\eta/D = 0$; see Fig. 2 for a definition of the coordinate system) from the low velocity region near the bubble wake. A similar behavior is observed for conditions EB1 and EB3, cases in which the bubble wake is visible at the measurement station. The liquid film for condition EB3 reaches 80% of the pipe cross section. For condition EB1, Fig. 14a shows that the low velocity region near the upper wall is due to

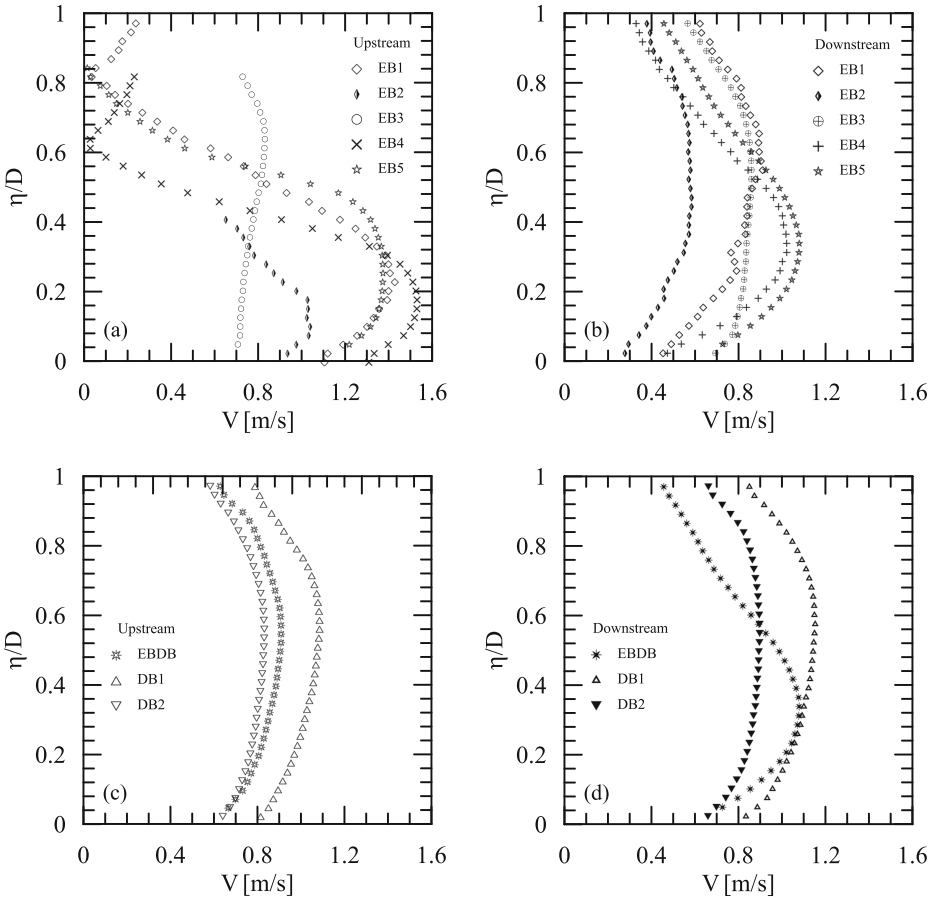

Fig. 14 Mean velocity profiles measured at stations 1 and 2 (Fig. 2 for a definition of the coordinate system) for EB conditions (**a,b**) and for EBDB and DB conditions (**c,d**)

the presence of slow dispersed bubbles detached from the wake of the long bubble. For the other conditions, EBDB, DB1 and DB2, uniform mean velocity profiles are observed at the upstream station (Fig. 14c).

Downstream of the junction, conditions EB4, EB5 and EBDB show a maximum velocity located near $\eta/D = 0.35$ (Fig. 14b,d). The smaller velocities observed on the upper region of these profiles ($0.6 \leq \eta/D \leq 1$) show the effect of the unsteady separation region described previously in Fig. 10. Uniform mean velocity profiles are observed for the other conditions.

The size distributions of small bubbles downstream of the T-junction are shown in Fig. 15. This analysis is conducted for a region immediately downstream of the junction, as shown in Fig. 2. The lines shown in Fig. 15 are log-normal distributions fitted to the experimental data. The distributions are expressed through relative frequency histograms. The mean equivalent bubble diameter is defined as the mean diameter of spherical particles that would have the same surface area as the measured object. Log-normal distributions are reputedly the commonest size distributions for bubble flow (Ribeiro Jr. and Lage [24], Frederix et al. [25]) and even for large bubbles in slug flow (Gonçalves et al. [26]).

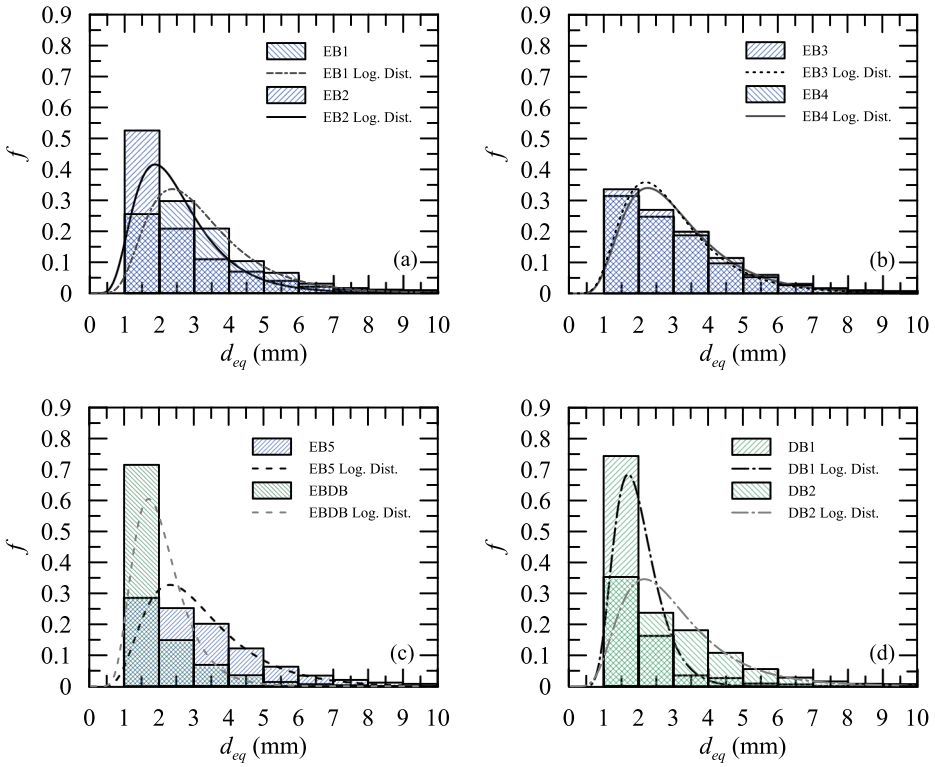

Fig. 15 Bubble size distribution downstream of the junction for conditions listed in Table 1

Figure 15 shows that, for all investigated conditions, bubbles with diameters under 6 mm are predominantly observed downstream of the T-junction. These bubbles result from the physical processes above described and are intrinsic to the flow dynamic parameters and geometry. The peak value of the log-normal size distributions of bubbles that are carried away with the liquid phase in the inclined pipe ranges from 1.6 mm for condition DB1 (Fig. 15d) to 2.5 mm for condition EB5 (Fig. 15c). Of course, high liquid flow rates tend to carry more bubbles downstream, increasing the observed frequency of small diameters. For the higher gas fraction conditions, tests EB1 and EB3 (Fig. 15a,b), the size distributions are slightly shifted towards higher diameters.

The velocities of dispersed bubbles U_b and V_b are presented in Fig. 16 (referred to the fixed PIV coordinate system x,y (Fig. 2)). All the lines in Fig. 16 are normal distributions fitted to the measured data, expressed as relative frequency histograms. Figure 16a shows U_b for the different elongated bubble flow patterns, while Fig. 16b presents the results for the transition and dispersed bubbles conditions. For the lower mixture velocities, EB2 and EB4, the distributions are approximately centered on a peak of 0.4 ms^{-1}. For higher mixture velocities, all the velocity distributions are very similar, with peak velocities around 0.8 ms^{-1}. A comparison of the range of the velocity distribution of U_b with the values shown in Fig. 14 (referred to the coordinate system ξ, η; differences in velocities referred to both coordinate systems are about 2%) indicates that the small bubbles follows the velocity of the bulk liquid flow. Negative values of U_b denote the small bubbles are moving towards the

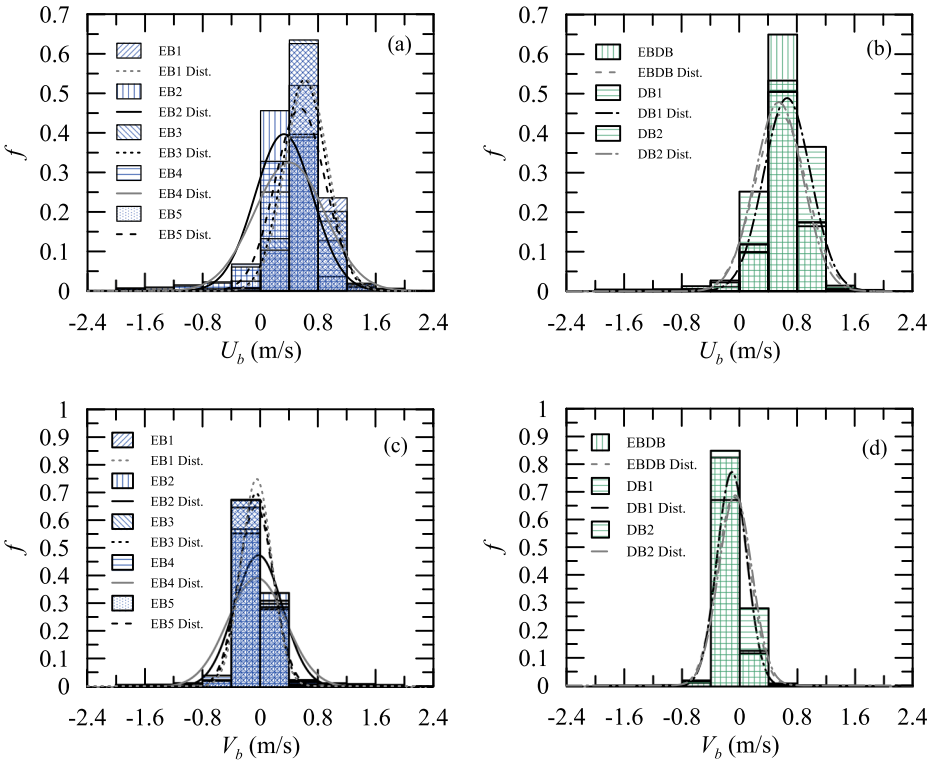

Fig. 16 Bubble velocity distributions for conditions listed in Table 1

T-junction. This shows that only few bubbles, when trapped inside the recirculation region (Fig. 10), have a tendency to move on the opposite direction in relation the main flow.

The vertical component of the bubble motion, V_b, presented in Fig. 16c and d, is shown to have a normal distribution centered around zero. This shows that bubbles below 6 mm diameter are not affected by gravity so that buoyancy forces do not contribute to the phase separation process.

3.3 Flow split

The flow split at the junction was evaluated through a balance of mass at the inlet and at the gas (vertical branch) and liquid (downward inclined) outlets. For the range of 1.9 $m^3h^{-1} \leq Q_{G_1} \leq 4.5$ m^3h^{-1} and 8 $m^3h^{-1} \leq Q_{L_1} \leq 11.3$ m^3h^{-1}, no liquid flow is observed at the vertical branch ($Q_{L_3} = 0$) so that liquid level remains stable.

For high flow rates, in the range of 10 $m^3h^{-1} \leq Q_{L_1} \leq 14$ m^3h^{-1} and 1.7 $m^3h^{-1} \leq Q_{G_1} \leq 7.5$ m^3h^{-1}, a portion of liquid is directed to the vertical branch. Stratified flow patterns at the entrance are always observed for these test conditions.

Figure 17 compares the gas flow rates at the inlet Q_{G_1} and at the outlet of the vertical branch Q_{G_3} for different liquid flow rates when $Q_{L_3} = 0$. The solid line represents a complete separation of the gas phase. The highest flow split is approximately 0.85 for the highest tested gas flow rates. As expected, the gas separation efficiency decreases as the liquid flow rate increases, since the gas bubbles are pushed away by the liquid momentum.

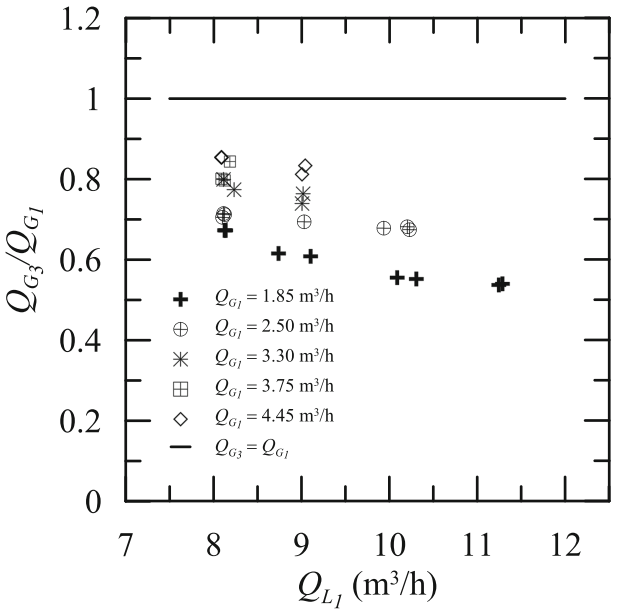

Fig. 17 Fraction of gas separation at the T-junction for different liquid flow rates and $Q_{L_3} = 0$

In other words, the residence time of a bubble passing through the T-junction is not high enough to permit its extraction through buoyancy effects.

Figure 18 shows the behavior of the liquid split at the junction according to a range of inlet liquid flow rates Q_{L_1}. The highest gas separation is obtained for $Q_{L_1} = 9$ m^{3}h^{-1}

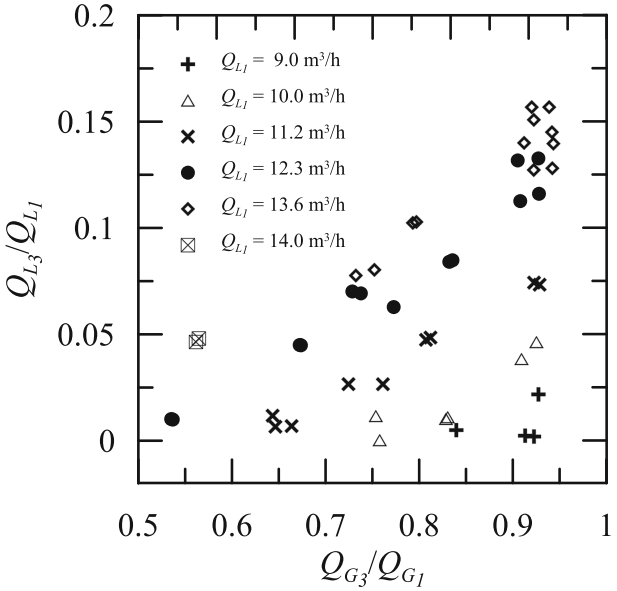

Fig. 18 Fraction of liquid split at the T-junction for different gas split ratios Q_{G_3}/Q_{G_1}

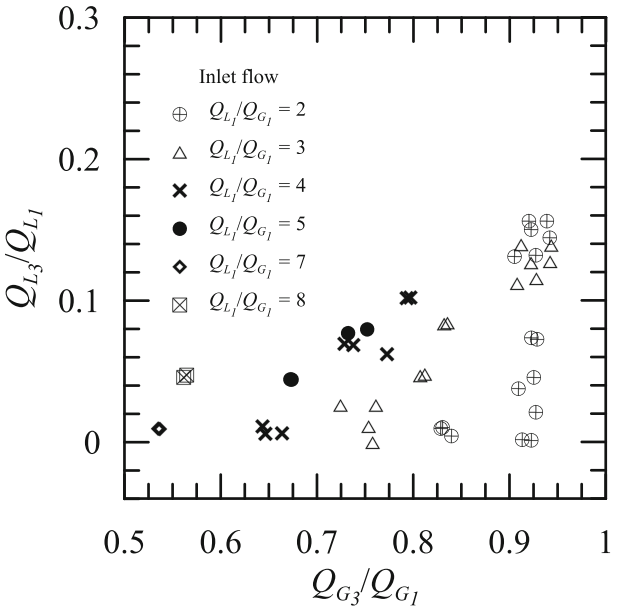

Fig. 19 Influence of the liquid-gas flow rate ratio on the split at the junction

(about 93%); in this condition, a very low fraction of liquid is carried out with the gas. The same efficiency can be achieved with higher liquid flow rates, up to 13.6 m^3h^{-1}, but the fraction of liquid carried over increases to 15%.

The flow split in the inclined T-junction for different ratios of liquid and gas flow rates is presented in Fig. 19. This figure summarizes the flow split fractions at the inclined junction for a range of operational conditions. The investigated configuration provides a satisfactory gas separation, up to 94%, with a maximum of 16% of liquid carried with the gas.

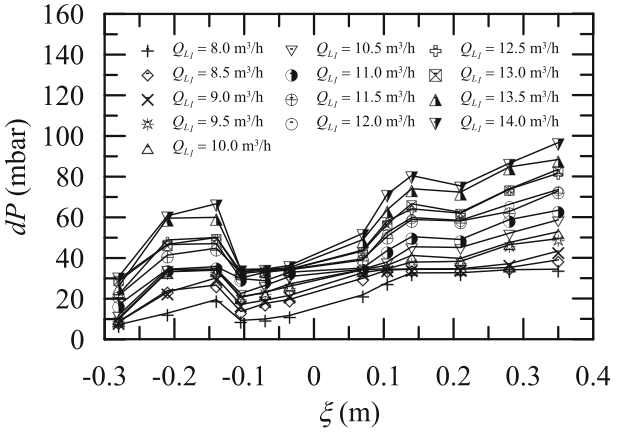

Fig. 20 Pressure drop along the T-junction for single phase flows. For coordinate system definition see Fig. 2

3.4 Pressure drop

Pressure drop distributions are discussed next. Figure 20 shows the pressure distribution along the inclined pipe for different liquid flow rates. The influence of the junction is clearly noted for $-0.1 \leq \xi(m) \leq 0.1$. The T-junction is positioned at $\xi = 0$ m.

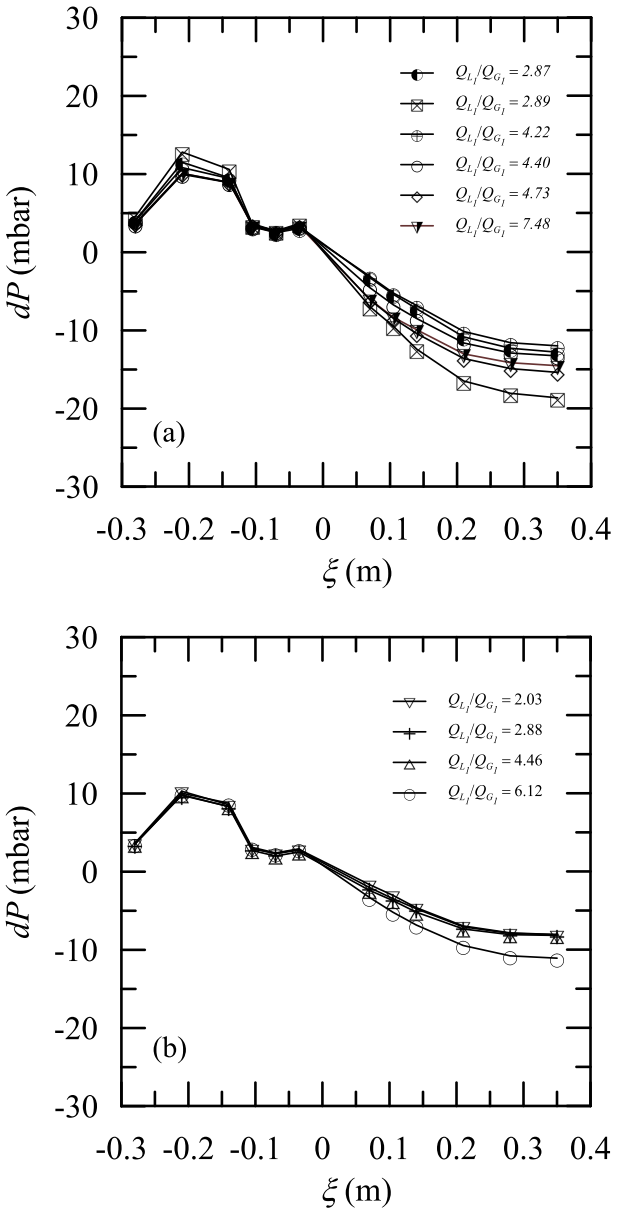

Fig. 21 Pressure drop along the T-junction for gas-liquid flows: **a** $Q_{L_3}/Q_{L_1} \neq 0$ and **b** $Q_{L_3}/Q_{L_1} = 0$. For coordinate system definition see Fig. 2

Figure 21 illustrates the pressure distributions for the cases with and without liquid carried over. The liquid split at the vertical branch (Fig. 21a) decreases the velocity at the downward inclined outlet pipe increasing the pressure drop for $\xi \geq 0$ m.

4 Final Remarks

The purpose of the present work was to investigate the behaviour of air-water flow mixtures across a particular type of 10°- downward inclined T-junction. The work has presented a detailed experimental campaign that provides a database which include global and local properties of the gas and liquid phases. Results are shown for mass flow rates at the entrance and exits, lengths and velocities of gas bubbles and mean and turbulent statistics of the continuous field. Particle Image Velocimetry and the Shadow Sizer technique were used simultaneously to provide information on the dynamics of the bubbles and the continuous velocity field. The geometry of the investigated T-junction is different from most works available in literature and the experimental results provide useful resource for the validation of computational fluid dynamics of junction flows.

For the flow rates described in Table 2, an elongated bubble flow pattern was observed at the downward inclined pipe. In particular, Taylor bubbles are oriented upwards and their positions are reasonably stable and fixed along the pipe. The height of the liquid column in the vertical branch remained stable except for a small intermittent level due to the rise of gas pockets that periodically separated from the long bubbles.

The work has shown that, as a long Taylor bubble is captured by the vertical branch at the junction, a break up mechanism due to shear forces causes the formation of small bubbles that follows the bulk liquid flow towards the end of the inclined pipe. This phenomenon was observed for all different test conditions investigated. The intermittent character of the break up mechanism was also discussed. A separation region and its bounding shear layer is created as a Taylor bubble is captured into the vertical branch and fades away as the incoming velocity profile is restored and the dynamic pressure force pushes the small bubbles downwards through the inclined pipe. This phenomenon poses a limitation to the T-junction when used for gas-liquid separation purposes.

Acknowledgments YSG is thankful to CAPES for a studentship and ANP/Petrobras for a research sponsorship. VYA acknowledges ANP/Petrobras for the award of a visiting scholarship. JBRL benefited from a CNPq Research Fellowship (Grant No 309455/2016-2) and from further financial support through Grants CNPq 458249/2014-9 and FAPERJ E-26/203.257/2016.

References

1. Shoham, O., Brill, J.P., Taitel, Y.: Two-phase flow splitting in a tee junction - experiment and modelling. Chem. Eng. Sci. **42**, 2667–2676 (1987)
2. Azzopardi, B.J., Smith, P.A.: Two-phase flow split at T-junctions: Effect of side arm orientation and downstream geometry. Int. J. Multiphase Flow **18**, 861–875 (1992)
3. Baker G.: Separation and Control of Gas-Liquid Flows at Horizontal T-junctions. PhD Thesis. Nottingham: University of Nottingham
4. Baker, G., Clark, W.W., Azzopardi, B.J., Wilson, J.A.: Transient effects in gas-liquid phase separation at a pair of T-junctions. Chem. Eng. Science **63**, 968–976 (2008)
5. Smoglie, C., Reimann, J., Muller, U.: Two-phase flow through small breaks in a horizontal pipe with stratified flow. Nuclear Eng. Des. **99**, 117–130 (1987)

6. Penmatcha, V.R., Ashton, P.J., Shoam, O.: Two-phase flow splitting at a T-junction with an inclined branch arm. Int. J. Multiphase Flow **22**(6), 1105–1122 (1996)
7. Azzopardi, B.: Measurements and observations of the split of annular flow at a vertical T-junction. Int. J. Multiph. Flow. **14**, 701–710 (1988)
8. Azzopardi, B.J., Hervieu, E.: Phase separation at T-junctions. Multiph. Sci. Tech. **8**, 645–713 (1994)
9. Azzopardi, B.J., Colman, D.A., Nicholson, D.: Plant application of a t-junction as a partial phase separator. Trans IChemE **80**, 87–96 (2002)
10. Wren, E., Azzopardi, B.J.: The phase separation capabilities of two T-junctions placed in series. Chem. Eng. Res. Des. **82**, 364–371 (2004)
11. Baker, G., Clark, W.W., Azzopardi, B.J., Wilson, J.A.: Controlling the phase separation of gas–liquid flows at horizontal T-junctions. AIChE J. **53**, 1908–1915 (2007)
12. Nogueira, S., Sousa, R.G., Pinto, A.M.F.R., Riethmuller, M.L., Campos, J.B.L.M.: Simultaneous PIV and pulsed shadow technique in slug flow: A solution for optical problems. Exp. Fluids **35**, 598–609 (2003)
13. Fu, T., Ma, Y., Funfschilling, D., Li, H.Z.: Dynamics of bubble breakup in a microfluidic T-junction divergence. Chem. Eng. Sci. **66**, 4184–4195 (2011)
14. Yamamoto, K., Ogata, S.: Effects of T-junction size on bubble generation and flow instability for two-phase flows in circular microchannels. Int. J. Multiphase Flow **49**, 24–30 (2013)
15. Caprini, D., Sinibaldi, G., Marino, L., Casciola, C.M.: A T-junction device allowing for two simultaneous orthogonal views: application to bubble formation and break-up. Microfluidics Nanofluidics **22:85**, 1–16 (2018)
16. Lahey, R.T.: Current understanding of phase separation mechanisms in branching conduits. Nuclear Eng. Des. **95**, 145–161 (1986)
17. Azzopardi, B.J.: Phase separation at T junctions. Multiph. Sci. Tech. **11**, 223–329 (2000)
18. Matamoros, L.M.C., Loureiro, J.B.R., Silva Freire, A.P.: Length-area-volume of long bubbles in horizontal slug flow. Int. J. Multiphase Flow **65**, 24–30 (2014)
19. JCGM, 2010: Evaluation of measurement data – Guide to the expression of uncertainty in measurement. Joint Committee for Guides in Metrology. JCGM 100:2008. 134 pp Corrected version (2010)
20. Barnea, D., Shoam, O., Taitel, Y.: Flow pattern transition for gas-liquid flow in horizontal and inclined pipes. Int. J. Multiphase Flow **6**, 217–225 (1980)
21. Barnea, D., Shoam, O., Taitel, Y.: Flow pattern transition for downward inclined two-phase flow: horizontal to vertical. Int. J. Multiphase Flow **5**, 735–740 (1982)
22. Spedding, P.L., Nguyen, V.T.: Regime maps for air water two phase flow. Chem. Eng. Sci. **35**, 779–793 (1980)
23. Kokal, S.L., Stanislav, J.F.: An experimental study of two-phase flow in slightly inclined pipes – I. Flow patterns. Chem. Eng. Sci. **44**, 665–679 (1989)
24. Ribeiro, C.P. Jr., Lage, P.L.C.: Experimental study on bubble size distributions in a direct-contact evaporator. Braz. J. Chem. Eng. **21**, 69–81 (2004)
25. Frederix, E.M.A., Cox, T.L.W., Kuerten, J.G.M., Komen, E.M.J.: Poly-dispersed modeling of bubbly flow using the log-normal size distribution. Chem. Eng. Sci. **201**, 237–246 (2019)
26. Gonçalves, G.F.N., Baungartner, R., Loureiro, J.B.R., Silva Freire, A.P.: Slug flow models: Feasible domain and sensitivity to input distributions. J. Petroleum Sci. Eng. **169**, 705–724 (2018)